

Plasmonic Au_xAg_y bimetallic alloy nanoparticles enhanced photoluminescence upconversion of Er³⁺ ions in antimony glass hybrid nanocomposites

TIRTHA SOM and BASUDEB KARMAKAR*

Glass Science and Technology Section, Glass Division, Central Glass and Ceramic Research Institute (CSIR, India), 196, Raja S. C. Mullick Road, Kolkata 700 032, India

Abstract

Er³⁺ ions and spherical (3-23 nm) Au_xAg_y bimetallic alloy (where x = 18-96 and y = 4-82, atom %) nanoparticles incorporated novel antimony oxide based reducing dielectric (glass) matrix, K₂O-B₂O₃-Sb₂O₃ (KBS), has been synthesized by a new single step methodology involving selective thermochemical reduction. Their absorption spectra show single tunable (536-679 nm) surface plasmon resonance band along with the typical absorption peaks of Er³⁺ ion. X-ray and SAED indicate the formation of (111) and (200) planes of Au_xAg_y alloy. The luminescence intensity of two prominent emission bands of Er³⁺ ions centered at 536 (green) and 645 (red) nm due to ⁴S_{3/2} → ⁴I_{15/2} and ⁴F_{9/2} → ⁴I_{15/2} transitions were observed to be strongly dependent on the Au_xAg_y nanoparticle composition. Both the bands undergo a maximum of 1.5 and 4.5 fold intensity enhancement respectively in presence of Ag₅₆Au₄₄ alloy (atom %) due to plasmon induced local field enhancement.

*Corresponding author. Email: basidebk@cgcricri.res.in

Tel.: +91-33 2473 3469; fax: +91-33 2473 0957

Keywords: Gold-silver alloy nanoparticles • Erbium (III) • Nanocomposite • upconversion • Enhanced fluorescence • Antimony oxide glass

1. Introduction

Frequency upconversion is the generation of short wavelengths visible or UV light from lower energy near-infrared (NIR) radiation involving at least two photons. Rare-earth (RE^{3+}) ion doped upconversion based materials have attracted considerable attention since the 1960s due to their promising applications in various areas of modern optics [1-3]. The Er^{3+} ion is one of the important active RE^{3+} ion used to obtain red and green upconversion emissions due to its favorable energy level structure [4-6]. Solid state red and green light sources are desirable for color displays, optical data storage, biomedical lasers and undersea optical communications [1-6]. But the absorption cross-section of the Er^{3+} ion is low. So to increase the upconversion efficiency, energy transfer from another species with a large absorption cross-section (such as Yb^{3+}) [7,8] or semiconductor nanocrystals like SnO_2 [9] has been employed. Very recently, use of plasmonic metal nanoparticles (NPs) and surfaces as platforms to enhance luminescence of RE^{3+} ions has been developed as a novel technique. Modification of the spontaneous isotropic and directional emissions of the emitter by surface plasmons of metal NPs, termed as nano metal enhanced luminescence (NMEL) or radiative decay engineering creates exciting opportunities with immense potential application in nanophotonics and nano-optics [10,11]. So, currently stable hard inorganic dielectrics, particularly glasses, co-embedding RE^{3+} ions and metal NPs are being developed and studied [12-27]. These materials with enhanced luminescence properties, particularly nano metal enhanced upconversion, are promising for plasmon controlled nanophotonic technologies like solar cells, light emitting diodes, advanced traffic displays, etc [10].

Metal NPs can influence the photoluminescence emission of RE^{3+} ions in several ways. Local field enhancement induced by surface plasmon resonance (SPR) of metal NPs has often been accentuated as the potential cause of fluorescence enhancement when the excitation or

emission is resonant or near the surface plasmon resonance (SPR) wavelength of metallic NPs [14,15,22]. SPR is an intriguing opto-electronic phenomenon exhibited by metal NPs embedded in dielectrics (here glass). The free conduction band electrons of the metal NPs collectively oscillates to and fro with respect to the positive core of the metal due to columbic attraction inducing a transient dipole in presence of light, and when the frequency of incident electromagnetic radiation is resonant with the frequency of electronic oscillation, SPR absorption occurs [10]. For noble metal NPs like Au and Ag, the SPR absorption band is in the visible region. In addition to absorption, these are intense light scattering and a tremendous enhancement of the local electromagnetic field around the metal NPs [10,11]. It is suggested that the distinctive local field enhancement may be so high that molecules in the vicinity of the plasmonic noble metal NPs (about 10 nm apart) may feel up to a 100 times more intense field as opposed to the direct excitation in a plasmon-free environment [17].

Besides, plasmonic metal nanostructures can modify the free-space conditions around the emitter due to their scattering effects [28]. The nanoparticle scattering is generally known to increase with increase in nanoparticle size. Other mechanisms include enhancement of radiative decay rate which modifies the quantum yield [10,29] and enhancement of photonic mode density [29]. Energy transfer from metal NPs to RE^{3+} ions has been accentuated as the potential cause when the SPR is non-resonant (out-of-SPR) with excitation or emission [18,19]. NMEL also depends on the relative separation between the RE^{3+} ion and the NP. At very short distance the presence of the metal leads to quenching of RE^{3+} luminescence due to creation of new non-radiative channels by light absorption inside the metal and energy transfer from the excited RE ion to the metal SPR [29].

The size, geometry and constitution of the NPs determine the characteristics of the localized surface plasmons it supports which in turn influence the NMEL process [10]. Anisotropic NPs and rugged surfaces of quasi-spheroidal nanostructures are more preferred aspirants for NMEL than spherical nanostructures because the local surface electron densities, induced by plasmonic oscillations, are drastically increased and confined near their spiky edges or rough surfaces, act as light-harnessing nano optical antennas converting visible light into large localized electric field (“lightning-rod effect”) and thereby increasing the local field effect tremendously [10]. Metal-enhanced luminescence has been mostly studied using silver NPs [12-26,29] and relatively less with Au NPs [27] due to the intense and narrow SPR peaks of Ag and it is suggested that silver is expected to exhibit higher enhancements than gold [30]. An important advantage of the bimetallic alloy nanoparticles is that their continuously tunable SPR band owing the possibility of composition changes in contrast to monometallic Au and Ag NPs which have relatively unchanging optical properties [31]. The new interesting surface characteristics may evolve from the combination of two kinds of metals and their fine structures and creates the opportunity for the plasmon modes to be resonant with emission and excitation wavelengths. Regarding the enhancement of local electric field, it is often suggested that stronger local-field enhancements are present near pure Ag and Au systems since their plasmon resonances are much stronger than the Au-Ag alloy [32,33]. Consequently, there are only few studies on bimetallic alloy NPs induced fluorescence enhancement [34,35].

Although the NMEL studies were initially taken up in sol-gel and melt-quench derived silicate glasses [15,18], but very recently serious emphasis is given to heavy metal oxide [20,21,24-27] and chalcogenide glasses [22] as hosts to conduct NMEL due to their low phonon energy which diminishes multiphonon relaxation and non-radiative loss and provides for

effective upconversion processes. The fabrication dielectric (glasses) matrices encapsulating nano scale monometallic and particularly inter-metallic particles encounter several difficulties like different chemical reactivities of two metals with the matrix, which can promote separation (via oxidation, for instance) instead of alloying of the species. Literature reports show several multi-stage approaches, such as sol-gel process, metal-dielectric co-sputtering deposition, sequential metal-ion implantation, pulsed laser deposition, dual ion-exchange and subsequent heat treatment at high temperatures in hydrogen atmosphere or UV-light, X-ray or laser irradiation, are used to incorporate thin layers of metal nanoclusters [31,36,37]. Consequently reports of bimetallic-glass composites are relatively few. To the best of our knowledge there is no report of effect of bimetallic alloyed nanoparticles on the photoluminescence properties of any RE^{3+} ion embedded within glass matrices. Therefore, simplification of preparation techniques to generate of new bulk dielectric (glass) matrices incorporating bimetallic NPs for plasmon enhanced luminescence investigation of RE ions can set a paradigm in the burgeoning discipline of applied plasmonics.

Among the heavy metal oxide glasses, we confine our attention on Sb_2O_3 based glass systems for photonic, particularly surface-plasmon-enhanced luminescence applications due to its two unique properties. Firstly, possesses low phonon energy (602 cm^{-1}) compared to conventional glass systems [7]. Secondly, it is not a strong reducing agent (Sb^{5+}/Sb^{3+} , $E^\circ = 0.648\text{ V}$) [38] and its selective reduction property can be utilized to synthesize nano bimetal:RE co-embedded (hybrid) nanocomposites. Here we have represented how these two properties of antimony glasses make them unique for photonic application in the family of glasses. It must also be emphasized that although bismuth, lead, tellurite and germanate glasses have been broadly studied for photonic applications [1,4-6,20,21,23-25] explored but the area of Sb_2O_3

based glasses and nanocomposites have remained largely unexploited. This is because the low field strength (0.73) of Sb^{3+} makes it a poor glass former [39]. Additionally the intense vaporization of Sb_2O_3 during melting and high devitrification during casting has made their synthesis very much difficult and only tiny pieces are usually obtained. It is only in recent times that by proper selection of base glass composition and melting techniques we first obtained monolithic antimony oxide glasses suitable for practical application [40]. So we could first exploited $\text{Au}:\text{Er}^{3+}$ and $\text{Ag}:\text{Er}^{3+}$ -antimony glass hybrid nanocomposites for nanophotonic application [26,27]. The principle behind the synthesis of these hybrid nanocomposites involved in-situ thermochemical reduction by employing the reducing property of Sb_2O_3 and metal cluster chemistry simultaneously. So, precise control of nanoparticles shapes and orientation within the disordered Sb_2O_3 matrix was not possible. Hence an independent study of the unusual optical properties of Au_xAg_y alloy NPs and Er^{3+} ions co-embedded in Sb_2O_3 glasses would be quite valuable to the scientific community.

In this paper, we demonstrate the single-step melt-quench approach for fabrication of bulk potassium boron antimony oxide glass $\text{K}_2\text{O}-\text{B}_2\text{O}_3-\text{Sb}_2\text{O}_3$ (KBS) co-doped with nano gold-silver Au_xAg_y alloy particles and Er^{3+} ions. We also attempt to realize the effect of Au_xAg_y alloy NPs on the upconversion fluorescence emissions (visible) of Er^{3+} under near infrared (798 nm) photoexcitation, explain the plasmonic controlled nanophotonics in these nanocomposites with the existing fundamental (electrodynamics) theories. X-ray diffraction (XRD) analysis and transmission electron microscopy (TEM) were also used to characterize the resultant nanocomposites.

2. Experimental details

2.1 Nanocomposite preparation

We used potassium metaborate, $\text{KBO}_2 \cdot x\text{H}_2\text{O}$ (15.7% H_2O , Johnson Matthey), antimony(III) oxide, Sb_2O_3 (GR, 99 %, Loba Chemie), chloroauric acid, $\text{HAuCl}_4 \cdot x\text{H}_2\text{O}$ (49 % Au, Loba Chemie), silver nitrate, AgNO_3 (99.9%, Exceller, Qualigens) and erbium(III) oxide, Er_2O_3 (99.99 %, Alfa Aesar) as the raw materials. 20 g base glass of composition (mol %) $15\text{K}_2\text{O}-15\text{B}_2\text{O}_3-70\text{Sb}_2\text{O}_3$ (KBS) was melted using these raw materials in a high purity silica crucible at 900°C in air for 10 min followed by a stir with a high purity silica glass rod. The molten glass was then cast into a carbon plate and properly annealed at 260°C and then very slowly cooled to room temperature at the rate of $1^\circ\text{C}/\text{min}$. The nanocomposites were prepared in a similar technique. All the dopants were used in excess as shown in Table 1. Samples of about 2.0 ± 0.01 mm thickness were polished for optical measurements.

2.2 Property measurement

The density of the glasses was measured by Archimedes method using toluene with an error of ± 0.7 %. A double-beam spectrophotometer (Lambda 20, Perkin-Elmer) was used to record the UV-Vis-NIR absorption spectra at an error of ± 0.1 nm. An X'pert Pro MPD diffractometer (PANalytical) operating at 40 kV and 30 mA was used to record the X-ray diffraction patterns of the bulk samples with step size 0.05° (2θ) and step time 0.5 sec, from 10 to 80° . Sample for TEM characterization was prepared by ultrasonication (dispersion) of powdered nanocomposite samples in acetone (the nanocomposites were powdered in agate mortar), placing a drop of the supernatant on a carbon coated copper grid and drying at room temperature. TEM was done using a Jeol (model JEM 2010) operating at an accelerating voltage of 200 kV. A fluorescence spectrophotometer (Fluorolog 2, Spex) employing a Xe lamp as excitation source and a

photomultiplier tube as detector was used to record fluorescence spectra at ± 0.2 nm error. The excitation slit (1.25 mm) and emission slit (0.5 mm) were kept same for all samples. All measurements were carried out at room temperature. The enhancement of luminescence was found to be reproducible for all samples.

3. Results and discussion

3.1 Principle of thermochemical reduction

A probable mechanism of selective thermo-chemical reduction of Au^{3+} and Ag^{1+} to Au^0 and Ag^0 respectively by Sb^{3+} but not reduction of Er^{3+} could be anticipated by considering the reduction potentials (E°) of the respective redox systems [38]. In principle, the E° of polyvalent elements in glass melts may be different from those in aqueous solutions and are temperature-dependent. Since the E° values for antimony glasses and other required species at high temperature are not available in the literature, therefore for simplicity of understanding, here we have used the room temperature E° for simple systems at equilibrium with air: $\text{Sb}^{5+}/\text{Sb}^{3+}$ ($E^\circ = 0.649$ V), $\text{Au}^{3+}/\text{Au}^0$ ($E^\circ = 1.498$ V), Ag^+/Ag^0 ($E^\circ = 0.7996$ V), $\text{Er}^{3+}/\text{Er}^0$, $E^\circ = -2.331$ V and $\text{Er}^{3+}/\text{Er}^{2+}$ $E^\circ = -3.0$ V [38]. However, the trend or movement of alteration of the E° values of different redox pairs at high temperature of the glass melt would not be different than in aqueous solution at room temperature.

Here the possible spontaneous reduction reactions are $3\text{Sb}^{3+} + 2\text{Au}^{3+} \rightarrow 3\text{Sb}^{5+} + 2\text{Au}^0$ ($E^\circ = 1.05$ V and calculated free energy, ΔG , (where $\Delta G = -nE^\circ F$ and is around -608 kJ) and $\text{Sb}^{3+} + 2\text{Ag}^+ \rightarrow \text{Sb}^{5+} + 2\text{Ag}^0$ ($E^\circ = 0.95$ V and calculated ΔG around -183 kJ). Thus, Sb^{3+} reduce Au^{3+} to Au^0 and Ag^{1+} to Ag^0 while it itself is oxidized to Sb^{5+} . Other reactions like $3\text{Sb}^{3+} + 2\text{Er}^{3+} \rightarrow 3\text{Sb}^{5+} + 2\text{Er}^0$ and $\text{Sb}^{3+} + 2\text{Er}^{3+} \rightarrow \text{Sb}^{5+} + 2\text{Er}^{2+}$ would have an E° values -6.61 and -6.65 V respectively, and ΔG values are positive) manifesting that these reactions are non-spontaneous

and thermodynamically not feasible. Thus Er^{3+} ion does not undergo any reduction. This is caused by the mild reducing property of Sb_2O_3 , that is, it is able to reduce only Au^{3+} and Ag^+ to their respective zerovalence states but is unable to reduce Er^{3+} to any of its lower valence state in the same glass melt. This exemplifies the selective or choosy reducing behavior of Sb_2O_3 , i.e., without reducing Er^{3+} . Since the concentration of the reducing agent (Sb_2O_3) is enormously large, it is assumed that all Au^{3+} and Ag^+ are reduced to Au^0 and Ag^0 states respectively.

3.2 Physical properties

The composition and some properties of monolithic nanocomposites are listed in table 1. There is a gradual increase in density with increase in dopant concentration. They nanocomposites display uniform intense coloration which indicates their potential use as decorative items as well. The progressive change in color of the nanocomposites is attributed to the different Au and Ag concentration ratios which results in shifting of the SPR band frequency in the visible region [31].

3.3 UV-Vis-NIR absorption

The UV-Vis-NIR absorption spectrum of 0.3 wt % Er_2O_3 doped glasses (figure 1, curve a) shows the presence of nine absorption bands due transitions arising from the ground state $^4\text{I}_{15/2}$ of Er^{3+} to high energy excited states. The energies associated with these $f \rightarrow f$ intrashell transitions of were recognized as per Carnall's convention of Er^{3+} ion in aqueous solution [41] and earlier studies of Er^{3+} -doped glasses [4-6]. The individual position of the absorption bands of Er^{3+} are stated in our previous work [7].

Each of the $\text{Er}^{3+}:\text{Au}_x\text{Ag}_y$ co-embedded nanocomposites (figure 1, curves b-e) displays a single well-defined broad SPR band as well as the typical absorption bands of the Er^{3+} ion. The alloy formation is indicated from the fact that the optical absorption spectrum shows only one plasmon band which is sensitive to the composition [31,36,42]. The SPR band experiences a distinctive red-shift from 536 to 679 nm with increasing concentration of Au depending on rising Au/Ag ratio since the Ag concentration is constant. The SPR absorption maxima red-shifts monotonically in between the absorption maxima of the two pure metals (Ag and Au) NPs in KBS antimony glass [26,27]. The absorption is higher as the metal concentration increases. This is because the increase of bimetallic Au_xAg_y NPs within the glasses greatly reduces the transmission in the visible range.

In the present case, for each of the alloys only one SPR band is detected and the absorption maximum was always located between the SPR of monometallic Au^0 and Ag^0 nanoparticles endorsing their alloy characters. On the contrary if they were in a physical mixture of monometallic Au^0 and Ag^0 nanoparticles they would have exhibited two absorption peaks corresponding to the monometallic Ag^0 and Au^0 nanoparticles [42]. If they were core-shell particles (like $\text{Au}_{\text{core}}\text{-Ag}_{\text{shell}}$ or $\text{Ag}_{\text{core}}\text{-Au}_{\text{shell}}$), only one plasmon peak corresponding to that of the shell metal would have been obtained. If the shell is not sufficiently thick and dense, the surface plasmon of the core can successfully interact with the outer electromagnetic field so two distinct SPR peaks corresponding to pure Ag^0 and Au^0 NPs are observed [42].

It is noteworthy that Au^0 and Ag^0 NPs embedded in sodalime silicate glasses, which have refractive index, n about 1.5, exhibits plasmon peak around 520 and 410 nm respectively [37] and display red and yellow color respectively. Consequently SPR peak of Au-Ag alloy NPs in sodalime silicate glass are tunable between these two extreme wavelengths. Our SPR bands are

radically red-shifted from this well-known range primarily due to the effect of the high refractive index of the matrix because our KBS antimony glass has refractive index of about 1.9477. Consequently Au_xAg_y emission bands are positioned in the emission range of Er^{3+} ions providing the opportunity of efficient coupling [16]. According to the Mie theory the position of the SPR band maxima (λ_{max}) of spherical noble metal (Au^0 and Ag^0) NPs is susceptible to changes in embedding medium refractive index (n) as [42]:

$$\lambda_{\text{max}}^2 = \frac{4\pi^2 c^2 m \epsilon_0 (\epsilon^a + 2n^2)}{N e^2} \quad (1)$$

where c is the speed of light, m is effective mass of conduction electrons, N is the free electron concentration, e is the electronic charge, ϵ_0 is the free space permeability and ϵ^a is the high frequency dielectric function of the metal. Although the bulk plasma frequencies of Au and Ag are identical but ϵ^a of Au and Ag are quite different because the interband transitions in gold extend across most of the visible spectrum. The red-shift of the absorption band is due to the perturbation of the d-band energy levels. It has been suggested that the optical dielectric function of the alloy particles can be regarded as a combination of the composition-weighted average dielectric function of Au and Ag in the form [43]:

$$\epsilon_{\text{alloy}}(v_{\text{Au}}, \omega) = v_{\text{Au}} \epsilon_{\text{Au}}(\omega) + (1 - v_{\text{Au}}) \epsilon_{\text{Ag}}(\omega) \quad (2)$$

where v_{Au} is the volume fraction of Au and $v_{\text{Ag}} = (1 - v_{\text{Au}})$ is the volume fraction of Ag. Increase in v_{Au} results in increase in the effective value $\epsilon_{\text{alloy}}(x_{\text{Au}}, \omega)$ and red-shift of absorption bands. This explains the shift of the SPR peak of alloy nanoparticles with its composition.

Besides the distinctive red-shift the SPR bands have also gradually broadened and become asymmetric with their tails extended up to 1100 nm. Such broadening and tailing of the SPR band are due to decrease in interparticle distance of the alloyed nanoparticles. It is known that as the interparticle spacing became smaller, interactions (efficient surface plasmon coupling)

between the closely spaced metallic particles significantly red-shifts the plasmon peaks signaling the generation of enhanced localized electric field [10].

3.4 TEM image analysis

A representative transmission electron microscopy (TEM) image of the nanocomposite ESG2 (figure 2a) show a very broad size distribution from 3 to 23 nm. It seems that some of the small singly dispersed spherical nanoparticles of similar sizes undergo aggregation and coalescence to yield larger clusters. It is supported by the fact that due to melting point depression of nanoparticles, they may behave like liquid droplets within the glass matrix and these small diffusible entities easily undergo coalescence. The coalescence could have occurred during the glass formation process and/or during the TEM investigation due to irradiation under high energy electron beam [44]. Coalescence occurs when two phase domains (nanoparticles) of essentially identical composition and similar size form a larger phase domain in contact with one another reducing the total interfacial area. In coalescence process the number of particles decreases continuously and the particles grow with time while the volume fraction of particles which represents the total volume of all the nanoparticles in solution remained essentially constant [45]. However a large particle size distribution (gradient) is also indirect evidence of the existence of the Ostwald ripening process where the larger particles grow at the expense of the smaller ones [46]. The classical model of growth and ripening assumes a distinct nucleation process followed by growth by monomer attachment from solution, that is, dissolution of small crystallites of sizes below some critical curvature and the re-deposition of the dissolved species (monomers) on the surfaces of larger crystals. The process ultimately results in complete dissolution of the small crystallites and formation of larger particles. The process occurs because

smaller particles have a higher surface energy; consequently their higher total Gibbs energy is higher than larger particles. This provokes their apparent higher solubility. Ostwald ripening being a diffusion controlled process could occur inside the glass at elevated temperatures [46]. Practically the reduction of HAuCl_4 and AgNO_3 to metallic Au and Ag by Sb_2O_3 is found to take place almost instantaneously at high temperature (at 900 °C during the melting) when the kinetic conditions are just favorable to allow it. The molten system containing very high amount of reducing Sb_2O_3 and high concentration of metal may be compared to a supersaturated solution (molten glass) with a separated phase containing the solute (Au and Ag). Initially the nucleation and growth of the metal nanoparticles possibly occur simultaneously. The nucleation rate drops after saturation while the growth is expected to continue till monodisperse large size nanoparticles are formed. But currently we are unable to provide a time dependent TEM study is expected to yield data in favor of Ostwald ripening. But it is most probable that the nanoparticles adopt different growth mechanisms based on their size- and morphology-dependent internal energies. The question of particle formation either inside glass during melting or induced via TEM is interesting and deserves further investigations but is beyond the scope of the present investigation.

The formation of near-spherical nanoparticles of uniform contrast in the TEM image indicates that the nano particles consist of Au_xAg_y alloys. This is supported by the fact that the TEM images of bimetallic Au@Ag core-shell NPs are known to display areas of contrasting density with the dark region attributable to gold and the light region attributable to silver [47]. Comparing the standard reduction potential values of Au ($\text{Au}^{3+}/\text{Au}^0$ $E^\circ = 1.498\text{V}$), and Ag (Ag^+/Ag^0 $E^\circ = 0.7996\text{ V}$), Au is first expected to reduce forming the core followed by the reduction and deposition of Ag. But the melting temperature (i.e. temperature of in-situ

thermochemical reduction) is very high $\sim 900^\circ\text{C}$. The nanoparticle alloying can, in principle, result from an increase in the diffusion coefficient of the metals at high temperature, because the melting point lowers as their size decreases [42]. The melting point of metal particles decreases rapidly once the diameter is less than 100 \AA , which means that alloying and surface diffusion of atoms will be more facile on nanosized particles than on bulk metal. The melting points of bulk Au and Ag are 1064.18°C and 961.78°C respectively [38]. Also, the atomic size of Ag (atomic radius = 144 pm) is same to that of Au (atomic radius = 144 pm), this results in an easy inter-diffusion between Au^0 and Ag^0 atoms and no strain is induced in forming the alloy NPs [42].

The selected area electron diffractogram (SAED), Fig. 2b, obtained for alloy encapsulated nanocomposites is of very little help in establishing the nature of alloy and particle morphology because the d-spacings of Au^0 and Ag^0 are very similar to one another but indicates the presence of Au-Ag nanocrystallites. The particles display distinct ring patterns manifesting their crystallinity. The diffraction pattern agrees well with the standard d-spacing values of both Au^0 and Ag^0 . Since the d-values for Au^0 , Ag^0 and their alloy lie within $\pm 1\%$ of each other due to their comparable atomic radii and chemical nature, consequently their SAED patterns are indistinguishable. The energy dispersive X-ray (EDX) analysis also hardly assists in establishing the nature of alloy and morphology of the nanoparticles embedded in large quantity of antimony glass host because the diameter of the beam is larger than the individual nanoparticles sizes.

3.5 X-ray analysis

Since Au^0 and Ag^0 have similar lattice constants (4.078 and 4.086 \AA respectively), routine X-ray diffraction is incapable to distinguish the alloy compositions [48]. But the X-ray diffractions permit to estimate the average crystallite sizes. Figure 3 compares the XRD patterns of the Er^{3+}

doped glass, E (curve a) which has an amorphous nature and bimetallic Au_xAg_y alloy nanoclusters - Er^{3+} co-embedded composites EGS1, EGS2, EGS3 and EGS4 (curves b, c, d and e respectively). The nanocomposites EGS1-EGS4 show prominent diffraction peaks of Au^0 and Ag^0 at $2\theta = 38.12^\circ$ ($d = 2.356 \text{ \AA}$) and 44.72° ($d = 2.031 \text{ \AA}$) which corresponds to the (111) and (200) Bragg's reflections from the face centered cubic (fcc) structures of Au^0 and Ag^0 nanocrystals (JCPDS card file nos. 4-0784 and 4-0783 respectively) embedded in KBS antimony glass matrix. The XRD spectrum manifests the reduction of Ag^+ to Ag^0 metal and Au^{3+} to Au^0 by the reducing glass matrix component Sb_2O_3 since any external reducing agent is not employed. The average diameter (D) Au_xAg_y nanocrystallites were calculated using Scherrer's formula:

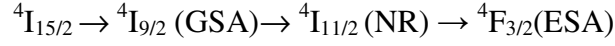
$$D = 0.9\lambda / FWHM \cos 2\theta \text{ (peak)} \quad (3)$$

where λ is the wavelength of X-ray radiation ($CuK\alpha = 1.5406 \text{ \AA}$), FWHM is the full width at half maximum at 2θ . The calculated average diameter of the Au_xAg_y nanocrystallites is found to be varied in the range 11-30 (± 1) nm. They are also listed in table 1. Another very interesting aspect observed from the XRD patterns is that at predominant concentration of Ag (ESG1), the (111) diffraction peak dominates while the formation of (200) planes is favored with addition of Au (ESG2-ESG4).

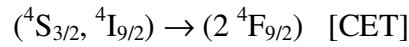
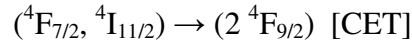
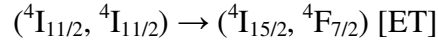
3.6 Enhancement of photoluminescence upconversion

Upconversion spectrum of 0.3 wt% Er_2O_3 doped KBS glass, under 798 nm excitation, is shown in figure 4 (curve-a). Three emission bands centered at 522 nm (green, weak), 536 nm (green, medium) and 645 nm (red, strong) due to ${}^2H_{11/2} \rightarrow {}^4I_{15/2}$, ${}^4S_{3/2} \rightarrow {}^4I_{15/2}$ and ${}^4F_{9/2} \rightarrow {}^4I_{15/2}$ transitions respectively are observed. At low concentration of Er^{3+} (0.3 wt %) the major

mechanisms are ground state absorption (GSA) followed by excited state absorption (ESA) [4-7]:



Other processes like energy transfer (ET) and cooperative energy transfer (CET) may also occurs between two Er^{3+} ions in the intermediate energy level as [4-7]:



These are shown in figure 5. The energy gaps of E_A (${}^4S_{3/2} \rightarrow {}^4F_{9/2}$) and E_B (${}^4F_{9/2} \leftarrow {}^4I_{9/2}$) are matched with a small red shift of 242 cm^{-1} . According to the Frank-Condon principle and lattice relaxation theory a small red shift between E_A and E_B is favorable for such type of energy transfer. The ${}^2H_{11/2}$ level is populated from the ${}^4S_{3/2}$ via thermal equilibrium between them which is very small at the experimental temperature. Consequently the band at 522 nm due to ${}^2H_{11/2} \rightarrow {}^4I_{15/2}$ transition has a very weak intensity (figure 4).

Luminescence intensity of both the 536 and 645 nm emission peak of Er^{3+} was observed to increase significantly in presence of bimetallic Au_xAg_y nanoparticles and attenuated at higher concentration of Au_xAg_y NPs. This behavior is illustrated in figure 4 (curves b-e) and 6, and table 2. Both bands have narrow full width at half maximum (FWHM $\sim 7 \text{ nm}$). We believe the primary reason for such fluorescence intensification of Er^{3+} ions is local field enhancement (LFE) induced by SPR of Au_xAg_y alloy NPs (as shown in figure 5) [10,14,15,20-27].

For a nanoparticle particles of diameter $D \ll \lambda$ wavelength of incident light, all the conduction electrons of the particle respond by collectively oscillating in phase and this oscillation has a $\pi/2$ phase lag with respect to the incident field. The electromagnetic waves

generated by plasmonic oscillations travel along the planar interface between a metal and a dielectric medium due to the mismatch between the dielectric function of the metallic nanoparticles and the encapsulating dielectric host (glass). Their concentration subwavelength distance scales gives rise to regions of giant energized local fields or “hot spots”, particularly at inter-particle junctions. Thus plasmonics enables electromagnetic (light) energy to be focused more tightly than the diffraction limit of light which applies to conventional optics [10,11]. This allows a resonantly enhanced dipolar field to build up around the particle [10,11]. So, at the SPR frequency, the field intensity in the near field of the nanoparticle is strongly improved relative to the incident optical wave. Within the quasistatic approximation, the electric field around a homogeneous and isotropic sphere with radius a can be written as [10,49]:

$$E_{out} = |E_0| \hat{X} - \alpha |E_0| \left[\frac{\hat{X}}{r^3} - \frac{3x(\hat{x}x + \hat{y}y + \hat{z}z)}{r^5} \right] \quad (4)$$

x , y , and z are the Cartesian coordinates, r is the radial distance, and \hat{x} , \hat{y} , and \hat{z} are the unit vectors. E_0 is the incident electromagnetic field vector pointing along the x -axis and independent of coordinates for distances on the order of the dimension of the sphere. The first term here is the applied field of the light and the second is the induced dipole of the polarized sphere. $\alpha(\omega)$ is the frequency dependent static metal polarizability [11,49]:

$$\alpha(\omega) = 4\pi a^3 \frac{\epsilon_{alloy} - \epsilon_m}{\epsilon_{alloy} + 2\epsilon_m} \quad (5)$$

Eq. (5) establishes SPR as a critical condition required for effective enhancement of external field. When the resonance condition is met, the real part of ϵ_{alloy} is $-2\epsilon_m$ and the imaginary part (ϵ_2) is small, α becomes large, producing an improved induced field [49]. It is also interesting to note that the plasmon resonance is not only determined by ϵ_{alloy} , but also by ϵ_m . At the plasmon

resonance, the near field of the nanoparticles is disturbed, thus such enhancements of the electromagnetic field at the interface are responsible for surface-enhanced optical phenomena [10,11].

The field enhancement factor, η can be defined as the ratio of the amplified local field and the incoming field, $|\eta(\omega)| = |E_{loc}| / |E_i|$ [11]. For a single nanoparticles, it can be written as the product of two factors $L=L_{sp}(\omega)L_{LR}$, highlighting the two possible enhancement factors— the surface-plasmon resonance of the whole particle (L_{SP}) and the lightning rod effect (L_{LR}) depending on extent of anisotropy. Hence the electric field around the plasmonic metal is increased. When the RE^{3+} ions are present within close ranges of such conducting metallic NPs, experience a drastic increase in their excitation rates by the induced enhanced near-electric field intensities (i.e. by local field enhancement) due to the modification of the free-space properties, leading to superior photoluminescence of RE^{3+} ions. The effect of this additional excitation field, $E_x = (E_{loc} - E_i)$, is shown in figure 5. Another factor responsible for photoluminescence enhancement is coupling of the Er^{3+} transition dipoles with resonant plasmon modes of Au_xAg_y NPs [16].

Another attractive observation was that under identical conditions, the pump excitation at 798 nm (NIR) induces the Au_xAg_y alloy doped nanocomposite to emit photons at 536 and 645 nm, having energy $\sim 18,657$ and $15,534 \text{ cm}^{-1}$ respectively (figure 4, curve-f). We believe that it is due to the inherent non-linear optical response of the dielectric host which is enhanced by several orders of magnitude by the incorporation of bimetallic clusters within the host matrices. Antimony borate glasses are known to possess non-linear properties with a large value of third order non-linear susceptibility (χ^3) which increases with Sb_2O_3 content [50]. The molar polarizability (as calculated from Lorentz-Lorenz equation) of KBS antimony glass of the

present study is found to be 9.598 \AA^3 which is considerably larger than conventional silica glass having molar polarizability of 2.965 \AA^3 . Besides heavy metal oxide glasses containing ions of high polarizability exhibit large non-linear optical properties [26,27,50]. Besides Au nanoparticles embedded in germane-silicate glass optical fibres exhibit visible and NIR photoluminescence due to radiative interband recombination between the sp and d-bands and radiative intraband transitions within the sp-band across the HOMO-LUMO gap respectively [51].

Therefore, some energy transfer (ET) from (weakly) fluorescent Au_xAg_y NPs to Er^{3+} ($\text{Au}_x\text{Ag}_y \rightarrow \text{Er}^{3+}$) can be considered. But, the intensity ratio data (table 2) suggests that the dramatic enhancement of upconversion peaks of Er^{3+} ions cannot be brought about only by feebly fluorescing Au_xAg_y NPs. Thus, photoluminescence emissions from Au_xAg_y NPs are likely to play a minor role and it may be a secondary additional excitation source of energy to Er^{3+} ions. This provides an opportunity to modify the photon density around the Er^{3+} ions and thereby increase the number of photons detected and captured by Er^{3+} [29]. Accordingly, the overall excitation in the upconversion process of Er^{3+} ions is stimulated by summation of the 798 nm NIR radiations, enhanced rate of excitation due to enhanced local field (major) induced by SPR and the absorption of emitted photons due to fluorescence of Au_xAg_y NPs by Er^{3+} ions, i.e., $\text{Au}_x\text{Ag}_y \rightarrow \text{Er}^{3+}$ ET (minor). As a result of superior excitation rate the population of the excited state of the Er^{3+} ions is expected to increase (by GSA and ESA) and subsequently the radiative decay rate is also thereby resulting in enhanced upconversion emission, as observed from figure 4. However, with the present experimental set-up (absence of life-time measurements facility) it is very difficult to account the dynamics of these contributions. Comparative intensity ratio data as shown in Table 2 is an alternative way to understand the said energy transfer [5, 7, 26, 27].

Table 2 compares the relative intensity of the green and red emission peaks of each of the nanocomposites. The local field steadily grows with alloy concentration until it saturates a very high concentration [10]. Although the local field enhancement factor reasonably explains the enhanced emissions of Er^{3+} ions but it cannot explain the drastic reduction of the emission bands of Er^{3+} at higher concentrations of alloy NPs. The damping of intensity (quenching) of the fluorescence peaks (figure 4 and table 2) is attributed to: (i) reverse energy transfer from Er^{3+} ions to Au_xAg_y NPs ($\text{Er}^{3+} \rightarrow \text{Au}_x\text{Ag}_y$) and (ii) plasmon re-absorption as a consequence of increased quantity of alloy NPs aggregates due to overlap of the broad tails SPR band of $\text{Au}_{96}\text{Ag}_4$ (SPR = 679 nm) with the emission peak of Er^{3+} [20-27]. The metal concentration dependence on the emission in intensities is illustrated in figure 6. The observed concentration dependence of luminescent intensities is results of the delicate balance between two competitive processes-the enhancing and quenching effects of Au_xAg_y NPs.

4. Advantages of this single-step technique

Although this versatile single-step approach eliminates precise size control over NPs sizes but it has several intriguing features such as: (1) the size and relative distance of the Au_xAg_y alloy NPs can be partially regulated by controlling the HAuCl_4 and AgNO_3 concentration of the batch; (2) the yield of Au_xAg_y alloy NPs (number density) is very high since it involves in-situ thermo-chemical reduction process. Consequently large enhancements of fluorescence properties of Er^{3+} (RE) ions are observed; (3) being a simple methodology, it can be potentially scaled up to relatively large quantities of material and bulk glasses embedded with alloy Au_xAg_y NPs can be obtained; (4) such stable luminescent nanocomposites are promising for high quality display devices (LCDs) particularly due to green and intense deep-red fluorescence having a narrow

FWHM (7 nm); (5) these intelligent nanocomposites may find other attractive optical applications in advanced solar cells and nanophotonic devices where infrared wavelengths may be converted and enhanced into useful visible wavelengths absorbable by inorganic solar cells; (6) all the NCs have tunable colors and can also be used for decorative purposes; (7) other interesting optical applications may be due to enhanced non-linearities caused by Au_{core}Au-Ag_{shell} NPs accompanied by intensified local electric fields around them.

5. Conclusions

Spherical bimetallic Au_xAg_y alloyed (where x = 18-96 and y = 4-82, atom %) nanoparticles (3-23 nm) coembedded with Er³⁺ ions in a new antimony glass (K₂O-B₂O₃-Sb₂O₃) monolithic nanocomposites have been synthesized by a new single-step approach without addition of any external reducing agent. The TEM images, SAED, XRD and plasmon band confirm the formation of the spherical alloyed nanoparticles. The XRD patterns show the presence of (111) and (200) crystallographic planes of fcc Au-Ag nano particles. The formation of Au_xAg_y alloy nanoparticles was monitored by the UV-Vis-NIR absorption spectroscopy which shows that the plasmon bands are slowly red-shifted from 536 to 679 nm between the peak positions of pure Ag⁰ and Au⁰ NPs and depending on increasing Au/Ag ratio. The UV-Visible absorption spectra also show characteristic absorption peaks of Er³⁺ ions. The photoluminescence upconversion of Er³⁺ excited at 798 nm show two prominent upconversion peaks at 536 and 645 nm arising due to due to ⁴S_{3/2} → ⁴I_{15/2} and ⁴F_{9/2} → ⁴I_{15/2} transitions respectively. Both the bands undergo a maximum intensity enhancement of 1.5 and 4.5 fold at in presence of Ag₅₆Au₄₄ alloy (atom %). The enhancement effect has been interpreted due to local field enhancement induced by Au_xAg_y SPR. Antimony oxide matrix plays a critical role of providing an excellent and convenient host

for producing bimetallic Au_xAg_y nanoparticles and stabilizing the Er^{3+} ions and the metallic nanoclusters. This study suggests that these $\text{Er}^{3+}:\text{Au}_x\text{Ag}_y$ antimony glass nanocomposites are a new generation intelligent functional nanomaterials and are potential candidate for applications as visible lasers, panel displays, solar cells and plasmonic devices particularly due to the high intensity of the deep-red fluorescence. We believe that this work would provide constructive new insights in the area of bimetallic-RE-antimony glass hybrid nanocomposites. **These interesting materials systems deserve further investigations (quantum yields, lifetimes, stability and growth mechanism) particularly in view of the fact that these composites have a wide range of possible but still unexplored applications.**

Acknowledgements

TS gratefully acknowledges the financial support of the Council of Scientific and Industrial Research (CSIR), New Delhi in the form of NET-SRF under sanction number 31/015(0060)/2007-EMR-1. They gratefully thank the Director of the institute for his kind permission to publish this work. The technical supports provided by the infrastructural facility (X-ray Division) of this institute and National TEM facility center, IIT Kharagpur, are also thankfully acknowledged.

References

- [1] F. Su, *J. Mod. Optics* **54** 2819 (2007).
- [2] P. R. Biju, G. Jose, P. V. Jyothy, V. Thomas and N. V. Unnikrishnan, *J. Mod. Optics* **52** 2687 (2005).
- [3] J. Méndez-Ramos, F. Lahoz, I. R. Martín, A. B. Soria, A. D. Lozano-Gorrín and V. D. Rodríguez, *Molecular Physics* **103** 1057 (2003).
- [4] H. Suna, S. Xua, L. Zhang, J. Wu, J. Zhang, L. Hu and Z. Jiang, *Mater. Sci. Eng. A* **394** 83 (2005).
- [5] B. Karmakar and R. N. Dwivedi, *J. Non-Cryst. Solids* **342** 132 (2004).
- [6] F. Su and Z. Deng, *J. Fluores.* **16** 69 (2006)
- [7] T. Som and B. Karmakar, *Opt. Mater* **31** 609 (2009).
- [8] G. E. Malashkevich, V. N. Sigaev, N. V. Golubevb, V. I. Savinkov, P.D. Sarkisov, I.A. Khodasevich, V. I. Dashkevich and A.V. Mudryi, *J. Non-Cryst. Solids* (2010), doi:10.1016/j.jnoncrysol.2010.09.007.
- [9] J. del-Castillo, V. D. Rodríguez, A. C. Yanes and J. Méndez-Ramos, *J. Nanopart. Res.* **10** 499 (2008).
- [10] P. N. Prasad, *Nanophotonics*, Wiley, New Jersey, pp. 129-151(2004).
- [11] S. A. Maier and H. A. Atwater, *Journal of Applied Physics* **98** 011101 (2005).
- [12] M. A. Noginov, G. Zhu, C. Davison, A. K. Pradhan, K. Zhang, M. Bahoura, M. Codrington, V. P. Drachev, V. M. Shalaev and V. F. Zolin, *J. Mod. Optics* **52** 1362 (2005).
- [13] S. M. Lee and K. C. Choi, *Opt. Exp.* **18** 12144 (2010).
- [14] O. L. Malta, P. A. Santa-Cruz, G. F. De Sá and F. Auzel, *J Lumin* **33** 261 (1985).

- [15] S. T. Selvan, T. Hayakawa and M. Nogami, *J Phys Chem B* **103** 7064 (1999).
- [16] J. Kalkman, L. Kuipers, A. Polman and H. Gersen, *Appl. Phys. Lett.* **86** 041113 (2005).
- [17] M. Eichelbaum and K. Rademann, *Adv. Funct. Mater.* **19** 1 (2009).
- [18] M. Matarelli, M. Montagna, K. Vishnubhatla, A. Chiasera, M. Ferrari and G. C. Righini, *Phys. Rev. B* **75** 125102 (2007).
- [19] J. A. Jiménez, S. Lysenko, H. Liu, E. Fachini and C. R. Cabrera, *J. Lumin.* **130** 163 (2010).
- [20] V. K. Rai, L. de S. Menezes, C. B. de Araújo, L. R. P. Kassab, D. M. da Silva and R. A. Kobayashi, *J. Appl. Phys.* **103** 093526 (2008).
- [21] T. A. A. de Assumpção, D. M. da Silva, L. R. P. Kassab and C. B. de Araújo, *J. Appl. Phys.* **106** 0635222 (2009).
- [22] Z. Pan, A. Ueda, R. Aga Jr., A. Burger, R. Mu and S.H. Morgan, *J. Non-Cryst. Solids* **356** 1097 (2010).
- [23] Z. Pan, A. Crosby, O. Obadina, A. Ueda, R. Aga Jr., R. Mu and S. H. Morgan, *Mater. Res. Soc. Symp. Proc.* **1208E** 009 (2010).
- [24] T. A. A. de Assumpção, D. M. da Silva, L. R. P. Kassab, J. R. Martinelli and C. B. de Araújo, *J. Non-Cryst. Solids* (2010), doi:10.1016/j.jnoncrysol.2010.02.016.
- [25] F. A. Bomfim, J. R. Martinelli, L. R. P. Kassab, T. A. A. Assumpção and C. B. de Araújo, *J. Non-Cryst. Solids* (2010), doi:10.1016/j.jnoncrysol.2010.03.028.
- [26] T. Som and B. Karmakar, *J. Appl. Phys.* **105** 013102 (2009).
- [27] T. Som and B. Karmakar, *J. Opt. Soc. Am. B.* **26** B21 (2009).
- [28] F. Tam, G. P. Goodrich, B. R. Johnson and N. J. Halas, *Nano Lett.* **7** 496 (2007).
- [29] M. Wu, J. R. Lakowicz and C. D. Geddes, *J. Fluores.* **15** 53 (2005).

- [30] J. Laverdant, S. Buil and X. Quélin, *J. Lumin.* **127** 176 (2007).
- [31] S. Pal and G. De, *Chem. Mater.* **17** 6161 (2005).
- [32] G. Pellegrini, G. Mattei, V. Bello and P. Mazzoldi, *Mater. Sci. Eng. B* **149** 247 (2008).
- [33] K. Kim, K. L. Kim and S. J. Lee, *Chem. Phys. Lett.* **403** 77 (2005).
- [34] S. Chowdhury, V. R. Bhethanabotla and R. Sen, *Appl. Phys. Lett.* **95** 131115(2009a).
- [35] S. Chowdhury, V. R. Bhethanabotla and R. Sen, *J. Phys. Chem. C* **113** 13016 (2009).
- [36] F. Gonella, E. Cattaruzza, G. Battaglin, F. D'Acaprio, C. Sada, P. Mazzoldi, C. Maurizio, G. Mattei, A. Martorana, A. Longo and F. Zontone *J. Non-Cryst. Solids* **280** 241 (2001).
- [37] H. Zeng, J. Qiu, S. Yuan, Y. Yang and G. Chen, *Ceram. Internat.* **34** 605 (2008).
- [38] D. R. Lide (Ed.), *CRC Handbook of Chemistry and Physics*, 75th edn, CRC press, Boca Raton, pp.8-21-34 (1975).
- [39] W. Vogel, *Glass Chemistry*, Springer-verlag, Berlin, (1992).
- [40] T. Som and B. Karmakar, *J. Non-Cryst. Solids* **356** 987 (2010).
- [41] W. T. Carnall, P. R. Fields and K. Rajnak, *J. Chem. Phys.* **49** 4424 (1968).
- [42] P. Mulvaney, *Langmuir* **12** 788 (1996).
- [43] K. S. Lee and M. A. El-Sayed, *J. Phys. Chem. B* **110** 19220 (2006).
- [44] H. Zheng, R. K. Smith, Y. -W. Jun, C. Kisielowski, U. Dahmen and A. P. Alivisatos, *Science* **324** 1309 (2009).
- [45] J. Polte, R. Erler, A. F. Thünemann, S. Sokolov, T. T. Ahner, K. Rademann, F. Emmerling and R. Kraehnert, *ACS Nano* **4** 1076 (2010).
- [46] D. Tatchev, A. Hoell, M. Eichelbaum and K. Rademann, *Phys. Rev. Lett* **106** 085702 (2011).

- [47] I. Srnova-Sloufova, F. Lednicky, A. Gemperle and J. Gemperlova, *Langmuir* **16** 9928 (2006).
- [48] G. C. Papavassiliou, *J. Phys. F: Metal Phys.* **6** L103 (1976).
- [49] A. M. Schwartzberg and J. Z. Zhang *J. Phys. Chem. C* **112** 10323 (2008).
- [50] L. A. Gómez, C. B. de Araújo, D. N. Messias, L. Misoguti, S. C. Zilio, M. Nalin and Y. Messaddeq, *J. Appl. Phys.* **100** 116105 (2006).
- [51] A. Lin, D. H. Son, I. H. Ahn, G. H. Song, W. T. Han, *Opt. Exp.* **15** 6374 (2007).

Table 1 Composition and some physical properties of the nanocomposites

Glass/ composite no	Composition ^a (wt %)			Compo- sition of alloy (atom %)	Density, ρ (g.cm ⁻³)	Visual color	SPR band	Particle diameter (D) calculated from Eq. 3 (± 0.1 nm)
	Er ₂ O ₃	Au	Ag					
E	0.3	-	-		4.573	Light pink	-	-
ESG1	0.3	0.003	0.007	Au ₁₈ Ag ₈₂	4.581	Violet	536	11
ESG2	0.3	0.01	0.007	Au ₄₄ Ag ₅₆	4.592	Pink	603	18
ESG3	0.3	0.03	0.007	Au ₇₀ Ag ₃₀	4.597	Light-blue	631	23
ESG4	0.3	0.3	0.007	Au ₉₆ Ag ₄	4.613	Blue	679	30

^a base glass composition (mol %) 15 K₂O-15B₂O₃-70Sb₂O₃

Table 2 Variation of relative intensity of upconversion fluorescence bands with Au_xAg_y composition in nanocomposites

Topic	Corresponding values				
Glass/composite number	E	ESG1	ESG2	ESG3	ESG4
<i>Upconversion ($\lambda_{ex} = 798$ nm)</i>					
Ratio of I ₅₃₆ at different concentration, ± 0.02	1	1.3	1.5	1.1	0.5
Ratio of I ₆₄₅ at different concentration, ± 0.02	1	3.1	4.4	2.2	1.2
Ratio of I ₅₃₆ : I ₆₄₅ at same concentration, ± 0.02	1:2.3	1:5.3	1:6.9	1:4.5	1:0.6

Figure Captions

Figure 1. UV-Vis-NIR absorption spectra of (a) E, (b) ESG1, (c) ESG2, (d) ESG-, and (e) ESG4 in the range of 380-1000 nm showing the various transitions of Er^{3+} arising from the ground state term $^4I_{15/2}$ and the SPR positions of bimetallic nano Au_xAg_y particles (thickness: 2 mm, for composition see table 1 and a. u. stands for absorbance unit).

Figure 2. (a) TEM image of the nanocomposite ESG2 showing spherical $\text{Au}_{44}\text{Ag}_{56}$ alloy nanoparticles embedded in antimony glass **showing wide distribution of particle sizes**, and (b) the corresponding SAED image (for composition see table 1).

Figure 3. XRD patterns of nanocomposites (a) E, (b) ESG1, (c) ESG2, (d) ESG3 and (e) ESG4 (for composition see table1).

Figure 4. Upconversion spectra of (a) E, (b) ESG1, (c) ESG2, (d) ESG3, (e) ESG4, (f) KBS glass doped with 0.007 wt% Ag and 0.01 wt% Au, and (g) base glass under excitation wavelength at $\lambda_{\text{ex}} = 798$ nm (for composition see table1 and amplification ratio table 2). The bases of the emission curves b-e have been uplifted for better visibility. Photon count per second is abbreviated as c.p.s.

Figure 5. Partial energy level diagram of Er^{3+} ion in $15\text{K}_2\text{O}-15\text{B}_2\text{O}_3-70\text{Sb}_2\text{O}_3$ (mol %) glass showing upconversion fluorescence emissions at 536 and 645 nm through ground state absorption (GSA), excited state absorption (ESA), energy transfer (ET) and co-operative energy transfer (CET) between Er^{3+} ions. Local field enhancement (LFE, E_x) by surface plasmon resonance (SPR) of Au_xAg_y alloy NPs and energy transfer (ET) from fluorescent Au_xAg_y NPs to Er^{3+} ions in nanocomposites are also shown (R and NR represent the radiative and nonradiative transitions respectively).

Figure 6. Plot of log intensity vs. concentration of Au (wt %) for 536 and 645 nm emission bands since the Ag concentration has been kept constant at 0.007 wt%. Maximum amplifications of both the 536 nm green and 645 nm red emissions is found to be about 1.5 and 4.5 folds respectively for composite ESG2 (for compositions see table1 and for amplification ratio refer table 2). Photon count per second is abbreviated as c.p.s. The lines are drawn to guide the eye.

Figures

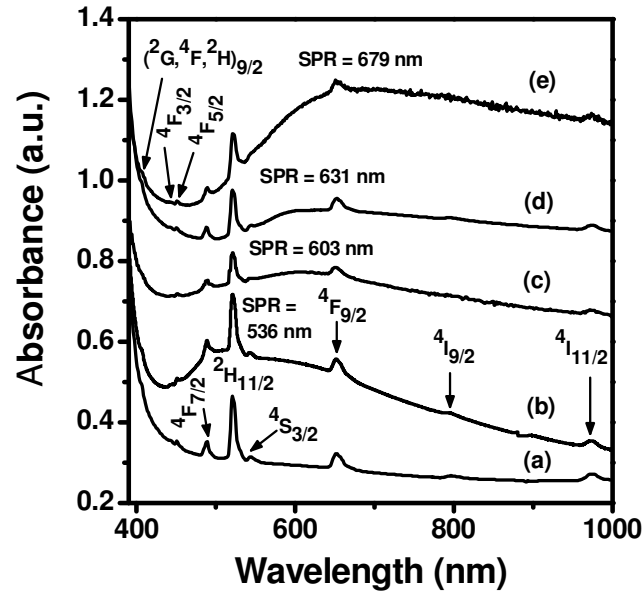


Figure 1. UV-Vis-NIR absorption spectra of (a) E, (b) ESG1, (c) ESG2, (d) ESG3, and (e) ESG4 in the range of 380-1000 nm showing the various transitions of Er³⁺ arising from the ground state term ⁴I_{15/2} and the SPR positions of bimetallic nano Au_xAg_y particles (thickness: 2 nm, for composition see table 1 and a. u. stands for absorbance unit).

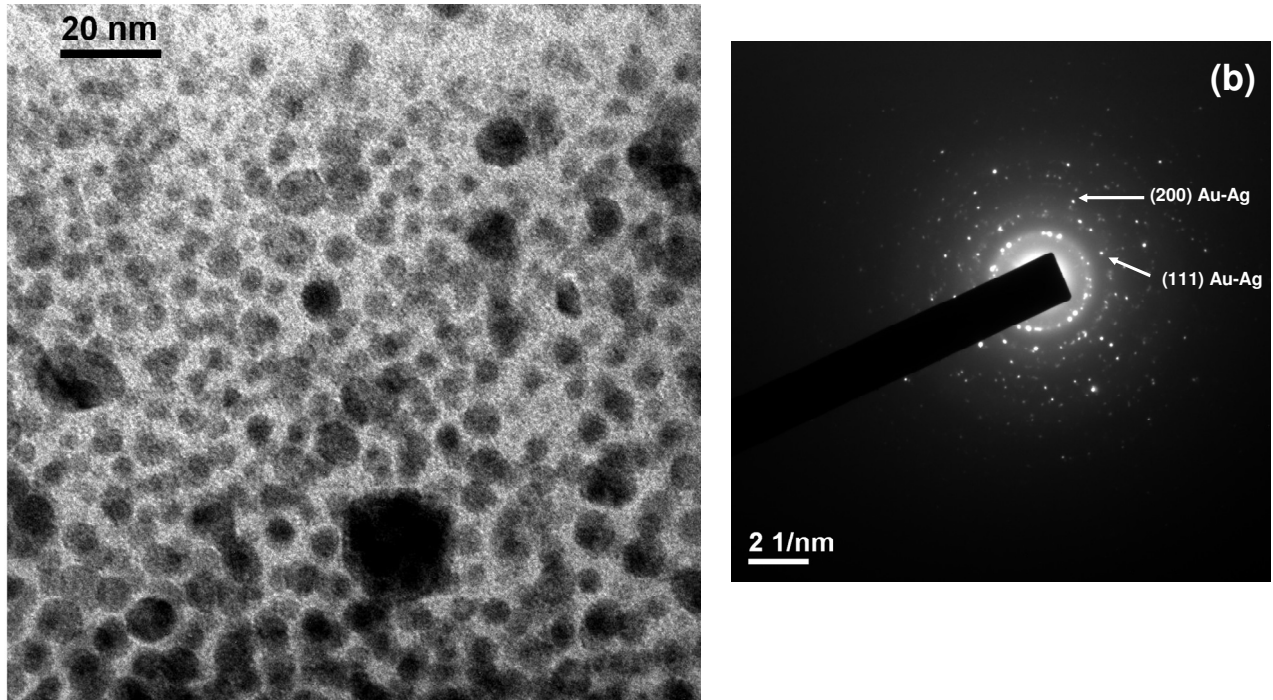


Figure 2. (a) TEM image of the nanocomposite ESG2 showing spherical $\text{Au}_{44}\text{Ag}_{56}$ alloy nanoparticles embedded in antimony glass showing wide distribution of particle sizes, and (b) the corresponding SAED image (for composition see table 1).

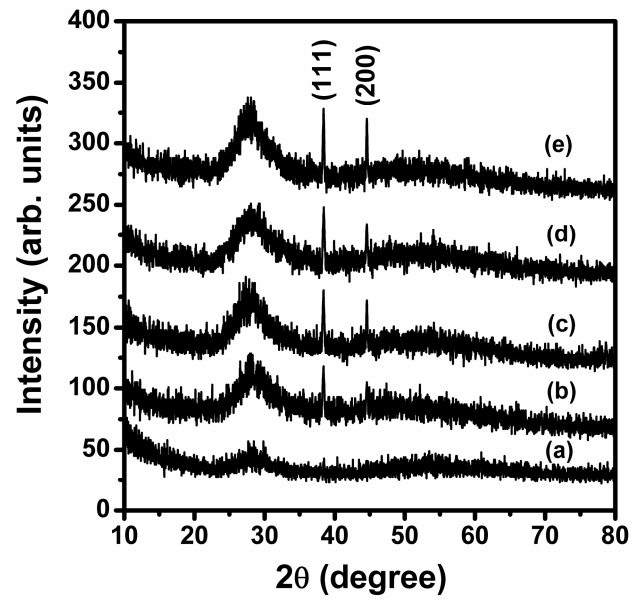


Figure 3. XRD patterns of nanocomposites (a) E, (b) ESG1, (c) ESG2, (d) ESG3 and (e) ESG4 (for composition see table1).

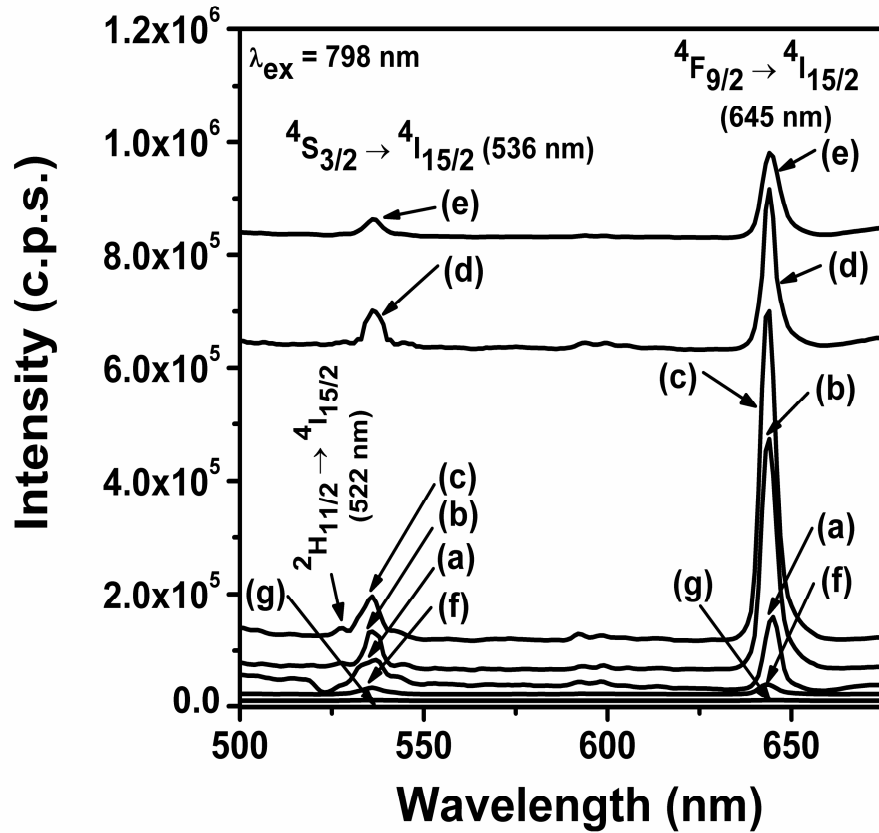


Fig. 4. Upconversion spectra of (a) E, (b) ESG1, (c) ESG2, (d) ESG3, (e) ESG4, (f) KBS glass doped with 0.007 wt% Ag and 0.01 wt% Au, and (g) base glass under excitation wavelength at $\lambda_{ex} = 798$ nm (for composition see Table1 and amplification ratio Table 2). The bases of the emission curves b-e have been uplifted for better visibility. Photon count per second is abbreviated as c.p.s.

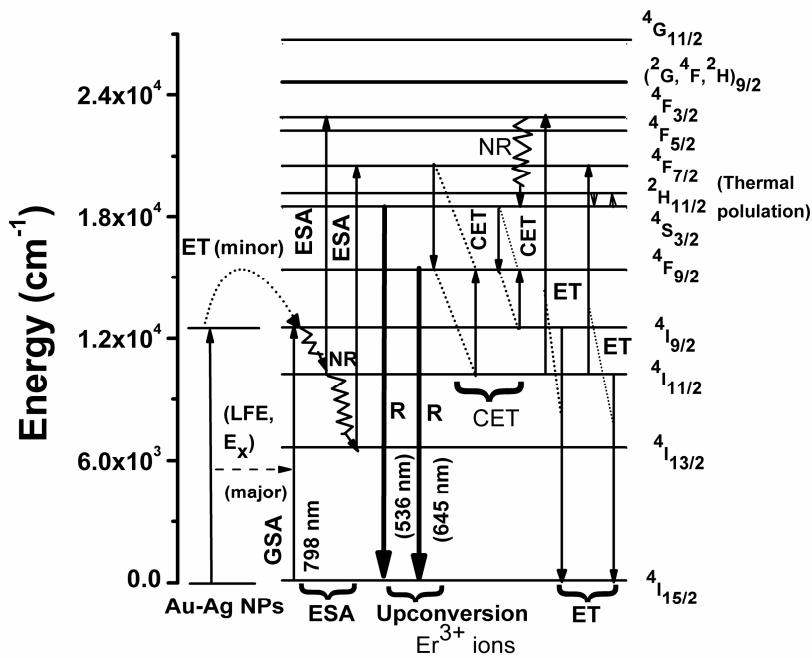


Figure 5. Partial energy level diagram of Er^{3+} ion in $15\text{K}_2\text{O}-15\text{B}_2\text{O}_3-70\text{Sb}_2\text{O}_3$ (mol %) glass showing upconversion fluorescence emissions at 536 and 645 nm through ground state absorption (GSA), excited state absorption (ESA), energy transfer (ET) and co-operative energy transfer (CET) between Er^{3+} ions. Local field enhancement (LFE, E_x) by surface plasmon resonance (SPR) of Au_xAg_y alloy NPs and energy transfer (ET) from fluorescent Au_xAg_y NPs to Er^{3+} ions in nanocomposites are also shown (R and NR represent the radiative and nonradiative transitions respectively).

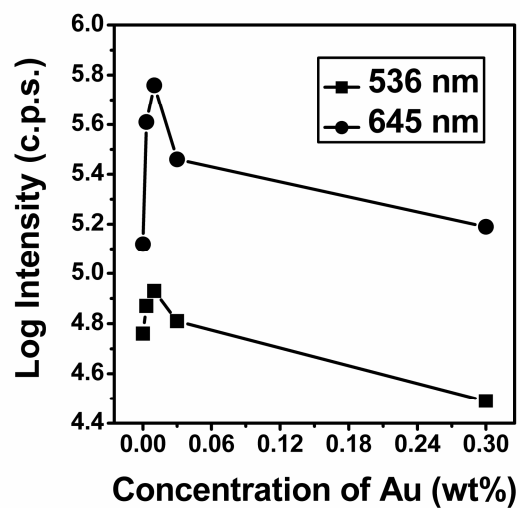


Figure 6. Plot of log intensity vs. concentration of Au (wt %) for 536 and 645 nm emission bands since the Ag concentration has been kept constant at 0.007 wt%. Maximum amplifications of both the 536 nm green and 645 nm red emissions is found to be about 1.5 and 4.5 folds respectively for composite ESG2 (for compositions see table1 and for amplification ratio refer table 2). Photon count per second is abbreviated as c.p.s. The lines are drawn to guide the eye.